Characterization and Application of Nanomaterials 2025, 8(2), 11613.
https://doi.org/10.24294/can11613

Article

Growth of 2D hexagonal boron nitride nanosheets on Ag using atmospheric pressure plasma for enhanced hardness

Muhammad Mudassar*, **Muhammad Shahid Rafique, Hafsa Mahmood, Muhammad Arslan, Tehreem Arshad, Ayesha Armani, Fakhar Siddiq, Maimoona Kanwal, Imran Shahadat, Fazila Javed**

Department of Physics, University of Engineering and Technology, Lahore 54890, Punjab, Islamic Republic of Pakistan
* **Corresponding author:** Muhammad Mudassar, mudassarmuhammadfraz7860@gmail.com

CITATION

Mudassar M, Rafique MS, Mahmood H, et al. Growth of 2D hexagonal boron nitride nanosheets on Ag using atmospheric pressure plasma for enhanced hardness. Characterization and Application of Nanomaterials. 2025; 8(2): 11613. https://doi.org/10.24294/can11613

ARTICLE INFO

Received: 20 March 2025
Accepted: 21 April 2025
Available online: 3 June 2025

Abstract: Two-dimensional hexagonal boron nitride nanosheets (h-BNNS) were synthesized on silver (Ag) substrates via a scalable, room-temperature atmospheric pressure plasma (APP) technique, employing borazine as a precursor. This approach overcomes the limitations of conventional chemical vapor deposition (CVD), which requires high temperatures (>800 °C) and low pressures (10^{-2} Pa). The h-BNNS were characterized using FT-IR spectroscopy, confirming the presence of BN functional groups (805 cm^{-1} and 1632 cm^{-1}), while FESEM/EDS revealed uniform nanosheet morphology with reduced particle size (80.66 nm at 20 min plasma exposure) and pore size (28.6 nm). XRD analysis demonstrated high crystallinity, with prominent h-BN (002) and h-BN (100) peaks, and Scherrer calculations indicated a crystallite size of ~15 nm. The coatings exhibited minimal disruption to UV-VIS reflectivity, maintaining Ag's optical properties. Crucially, Vickers hardness tests showed a 39% improvement (38.3 HV vs. 27.6 HV for pristine Ag) due to plasma-induced cross-linking and interfacial adhesion. This work establishes APP as a cost-effective, eco-friendly alternative for growing h-BNNS on temperature-sensitive substrates, with applications in optical mirrors, corrosion-resistant coatings, energy devices and gas sensing.

Keywords: 2D materials; Vicker's hardness; h-BN nanosheets (h-BNNS); borazine; surface chemistry; atmospheric pressure plasma (APP)

1. Introduction

Boron nitride (BN), a notable member of 2D materials, has been extensively investigated due to its excellent and desirable properties such as high surface toughness, low electrical but high thermal conductivity, surface hardness, versatile thermal and chemical stability, and impermeability to fluids [1–8]. h-BN is white, non-toxic, and impermeable, with a density of 2.27 g/cm^3, making it the least dense material in its class. White graphene is the term for the 2-D nanosheets of hexagonal boron nitride [9,10]. Owing to their interesting features, they offer considerable potential in a variety of applications, including coatings, stealth, automotive, gas sensing, aerospace, corrosion resistance, catalysts, energy storage, medicine, electronics, high-resolution imaging, water purification and flame retarding [11–17]. Boron nitride nanomaterials exhibit exceptional mechanical properties, including a fracture strength of 165 GPa and a Young's modulus of 0.8 TPa [18], alongside high thermal stability (up to 800 °C in air) [19–22] and a low thermal expansion coefficient (-2.72×10^{-6} K^{-1}) [23,24]. Their thermal conductivity (300–2000 $W \cdot m^{-1} \cdot K^{-1}$) [24,25] surpasses many conventional materials, making them ideal for thermal management applications. Unlike other 2D materials (e.g., graphene, MXene) [26–29], BN nanosheets (BNNS) are electrically insulative due to their wide bandgap (~5.6 eV), low leakage current, and high dielectric strength (12 MV·cm^{-1}) [30]. These properties enable BNNS-polymer nanocomposites to achieve superior performance in electronics, coatings, and energy devices [31–33]. Nanoscale BN is of potential use in nanostructured ceramic materials and nano-dimensional electronic devices [34–36]. h-BN is non-cytotoxic and contains an extent of biocompatibility [37,38]. Due to its electron affinity being highly negative [39], chemical, physical and thermal stabilities, the BN sheathing may function as an organic covering that is both protective and insulating for the materials it encapsulates. h-BNNS have several desirable qualities for potential uses in optics as well. It also has a significant field-emitting factor [40]. h-BNNS also exhibit desirable optical properties such as a direct band gap of 5.5 eV and great electromagnetic transparency, confirming its electrically insulating nature [41,42]. In lasers as well as LEDs, h-BNNS are utilized for heat dissipation and protective coating [43,44]. A protective layer of 130 μm thick h-BN was applied to a solar probe because of the outstanding stability of h-BN at high temperatures. It also contains high ratios of solar emissivity to absorptivity [45]. Unlike conventional bigger materials or thin films, 2-D boron nitride nanosheets can perform new or better functions. The distinctive anisotropy and mechanical characteristics of 2D materials have greatly spurred interest in their basic mechanics and optics as well as a broad range of applications [46–48]. Because of its high reflectivity in the UV-visible region, silver mirrors are an excellent choice for solar energy concentrators and astronomical telescopes [49,50]. Nevertheless, as a result of the reaction of Ag with sulfur-containing substances, particularly H_2S in the open atmosphere, Ag progressively tarnishes, creating black Ag_2S that reduces UV-VIS reflectivity and promotes electrical resistance. Ag_2S and can be removed using techniques like sanding and dipping in a sodium bicarbonate solution, but they also run the risk of irreversible material loss and the formation of micro-pits, which will eventually encourage more corrosion [51–53]. Atomic layer coating of conventional thin layers like AlO_x is also incompatible with metals like Ag because it can partially oxidize their surface and reduce their reflectivity [54,55]. While chromate conversion coatings and other tarnish inhibitors work well, they frequently include extremely toxic hexavalent chromium compounds [56]. In addition, the other carbon equivalents of boron nitride like graphene possess similar characteristics, however, a fatal drawback of graphene is that, with time, it may create a galvanic cell with the underlying metal Ag and potentially promote oxidation resulting in extended corrosion. These attributes make h-BNNS a suitable defensive coating that may be applied to Ag in challenging conditions. This work is the first to demonstrate such growth. Research on the CVD growth of h-BNNS on single [57,58], as well as polycrystalline Ag has been conducted [59], but no earlier studies have been made on the h-BNNS synthesis on industrially existing Ag utilizing a simple but versatile plasma facility [60]. Borazine has been used in chemical vapor deposition (CVD) to create nanoporous-like structures of h-BN on a variety metal surfaces, like Rh(111) and that of Ru(001) as well [61,62]. The main drawback of CVD (chemical vapor deposition) was that it requires a high temperature of 800 to 1600 °C and an extremely low pressure of 10^{-2} Pa which is industrially incompatible. Moreover, h- Boron Nitride nanosheets cannot be grown on all the substrates by CVD especially temperature sensitive substrates like plastics and polymers. Also, some chemicals like diborane, boron trihalides e.g., BCl_3, arsenic and phosphorus are highly toxic, explosive, and corrosive [63] at elevated temperatures and special care is required. Due to these reasons atmospheric pressure plasma is applied as it provides us the same growth at atmospheric pressure and room temperature. All the substrates from hard metals to soft polymers can be coated using non-thermal atmospheric pressure plasma. The plasma operating parameters, such as interelectrode spacing, power, interaction time, applied voltage and working gas pressure are easily adjustable. h-BNNS were synthesized on Ag through a simple plasma facility at room temperature and atmospheric pressure. The resulting h-BNNS were characterized using FT-IR analysis, FESEM analysis accompanied by EDS, XRD analysis, UV-VIS spectroscopy, and Vickers hardness tests.

2. Experimental setup

Figure 1 exhibits an illustrative schematic and an image of the atmospheric pressure plasma (APP) facility for the growth of h-BNNS on Ag substrates. Seven stainless steel capillary tubes act as the anode and are maintained at an elevated voltage to make up the reactor head. The cathode is mounted over a load-lock stage, horizontally aligned beneath the anode, and spaced 2 cm apart. These components are enclosed in an acrylic container with a top-mounted gas inlet pipe. The upper inlet provides nitrogen gas to the capillary tubes (cathode). A double-neck flask containing the precursor is attached to an argon (Ar) cylinder, which is then connected to the reactor head in order to transport the precursor fumes.

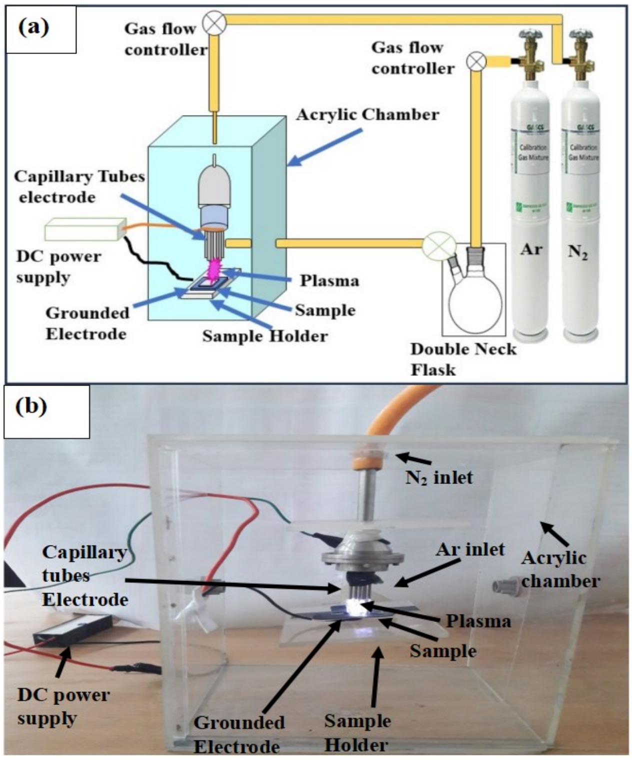

Figure 1. (a) An illustrative schematic; **(b)** an in-situ image of the atmospheric pressure plasma (APP) facility for h-BNNS growth on Ag.

Experimentation

h-BNNS were successfully grown on Ag with borazine (H_3BNH_3) serving as the precursor. For this purpose, commercially available Ag (99.9 % pure) with the dimensions of 8 × 8 × 2 mm^3 was used as a substrate. To ensure that the substrate was free from surface contaminations, it was washed in ethyl alcohol for two hours prior to treatment. Subsequently, the substrate was placed in an airtight desiccator to protect it from ambient exposure. Borazine (H_3BNH_3) was used as a boron nitride precursor. Ar was used as a precursor carrier gas while N_2 was used to produce plasma. 250 mL of borazine was filled in the double-necked flask having a capacity of 500 mL. The substrate Ag was placed on a horizontally mounted cathode. The argon was made to flow at a fine-tuned flow rate of 10 sl/m via the double-necked flask to carry the borazine fumes to the substrate. The N_2 was made to flow via the steel capillaries at an optimized flow rate of 10 sl/m. A 10 kV constant DC voltage was applied to the electrodes to generate the plasma. This resulted in the exposure of the substrate to fumes containing the precursor, coupled with plasma. In this way, nanosheets of h-BN were grown on Ag for 10, 15 and 20 min. In order to make a comparison, one Ag sample was kept untreated. For ease, the samples have been labeled as follows: pristine Ag sample as (Ag), 10 min. grown sample as (Ag GT)10, 15 min. grown samples as (Ag GT)15 and 20 min. grown samples as (Ag GT)20 respectively (where GT stands for "growth time").

FTIR evaluation was performed to confirm the presence of BN bonds and vibrational modes at the surface of grown samples. FESEM along with EDS was employed to evaluate microstructure and elemental analysis. XRD was implied to govern the hexagonal structure of BNNS. Diffused reflectance spectra were carried out to check the reflectivity of the samples. To confirm the hardness enhancement, the samples underwent Vickers hardness tests post-growth.

3. Results and discussions

3.1. FTIR analysis

FTIR analysis was performed to determine the presence of BN functional groups on substrate Ag. **Figure 2** shows the FTIR spectra for (Ag), (Ag GT)10, (Ag GT)15, and (Ag GT)20. The resolution was set at 2 cm^{-1}, with a frequency range spanning from 500 to 4000 cm^{-1}. Two prominent absorption bands, located at 805 cm^{-1} and 1632 cm^{-1}, are visible for (Ag GT)10, (Ag GT)15, and (Ag GT)20, confirming the presence of h-BN functional groups. The dotted boxes in **Figure 2** draw attention to the absence of these bands in (Ag). Depending on the type of BN structure, these peaks' precise locations vary. In h-BN, a prominent peak appears at approximately 805 cm^{-1}. These bands represent, respectively, the bending and stretching modes of the crystalline h-BN lattice bound to sp^2 [63–65]. As plasma exposure time increased, IR light reflection, associated with that of BN functional groups, intensified. This enhanced reflection is proportional to the enhanced BN formation for (Ag GT)20. This phenomenon can be explained by the decrease in pore size, surface roughness, and particle size, which leads to a greater reflection of IR radiation (also verified in SEM section). The BN structure, as well as the existence of impurities or structural defects, can all affect the exact location and form of this peak. Furthermore, other functional groups, such as C–H, C≡N, and C–C, which correspond to peak locations at 1367, 2265, and 2920 cm^{-1}, arise with longer plasma exposure time [66]. Since the experiment was conducted in the ambient environment, these groups might have arisen from environmental contamination. Upon comparison, it can be seen that the h-BNNS grown on Ag at an operating voltage of 10 kV for 20 min are the best among the others.

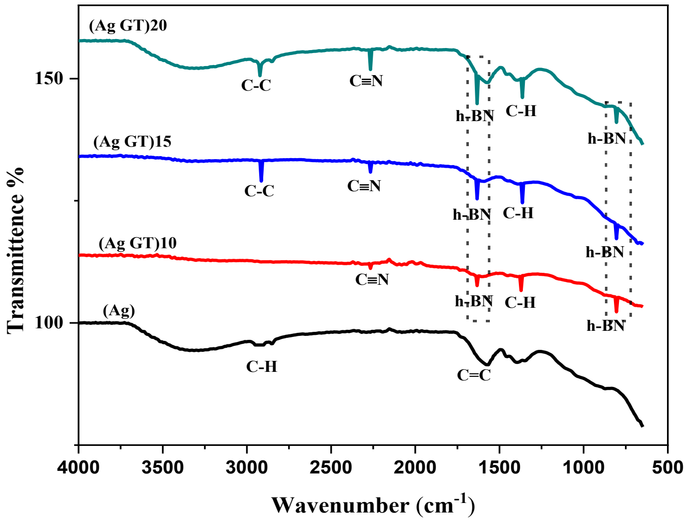

Figure 2. FTIR spectra of (Ag), (Ag GT)10, (Ag GT)15, (Ag GT)20. Dotted rectangles represent the distinctive bands of h-BN.

3.2. Scanning electron microscopy analysis

Having confirmed the presence of h-BN functional groups via FTIR, we next examined the morphological evolution of the nanosheets using SEM. **Figure 3** shows the scanning electron micrographs alongside EDX spectra for (Ag), (Ag GT)10, (Ag GT)15, and (Ag GT)20 respectively. Pristine Ag used as a substrate (**Figure 3a**) does not show any deposition; however, a few scratches are seen on the surface. **Figure 3b** reveals the surface morphology of h-BNNS grown via plasma operated for 10 min. There are uniformly distributed nanosheets of BN (**Figure 3b**). The high-energy atmosphere of plasma boosts the polarization exhibited by the covalently bound SP2 [67] h-BN. This enhanced polarization of the h-BN bond is a consequence of plasma bond interaction. As a result, electrostatic induction in the Ag substrate takes place, increasing the adhesion between the adsorbing BN particles and substrate Ag. Additionally, huge and unreacted particles are observed over the surface of these h-BNNS. These particles remained so because there is a layer (nanosheet of BN) between these bigger particles and substrate Ag, due to which these particles could not interact with the substrate. Also, the plasma exposure time was small, as a result they remained bigger. The existence of B and N was certified through the respective EDS spectrum. For (Ag GT)15 (**Figure 3c**), the BN nanosheets are more uniformly dispersed compared to (Ag GT)10. This is attributed to the enhanced plasma exposure with the fumes containing the precursor, which leads to greater electrostatic induction, ultimately increasing the electrostatic interaction between adsorbing BN particles and the underlying substrate Ag. For (Ag GT)15, big unreacted precursor particles are less abundant on the surface of h-BNNS, as the plasma has sufficient time to break them down. EDS examination verified the existence of B and N. **Figure 3d** displays the morphology of (Ag GT)20, where the SEM image shows that the BN nanosheets (as confirmed by EDX) appear to be fused or adhered, likely because of the extended plasma exposure with both the adsorbing BN particles and that of Ag. Plasma enhances interfacial properties, including inter-diffusion and the formation of BN surface layers, such as inter-diffusion and plasma-enhanced surface layers of BN. As the plasma exposure time increases, so does the electrostatic induction, resulting in stronger attraction between BN and Ag. Additionally, a few cracks can be observed in the h-BNNS in the FESEM micrograph of (Ag GT)20. These cracks likely formed after prolonged plasma heating, followed by rapid condensation when the samples were cooled to room temperature after the growth process. Boron nitride nanosheets interact strongly with Ag via van der Waals attractions as well as Coulombic forces [68]. The underlying Ag substrate appears as dark regions in the FESEM micrographs (as illustrated in **Figure 3b–d**), on the other hand, h-BNNS exhibits different shadows of grey. Since h-BN is a semiconductor or insulator, the electron charging from the FESEM beam causes the nanosheets to appear brighter. Upon comparison, distinct differences in the morphology of these nanosheets are observed. As plasma growth time increases, the sheets become more uniform. Consequently, (Ag GT)20 shows more uniform h-BNNS as compared to the others, which is attributed to the prolonged plasma exposure time.

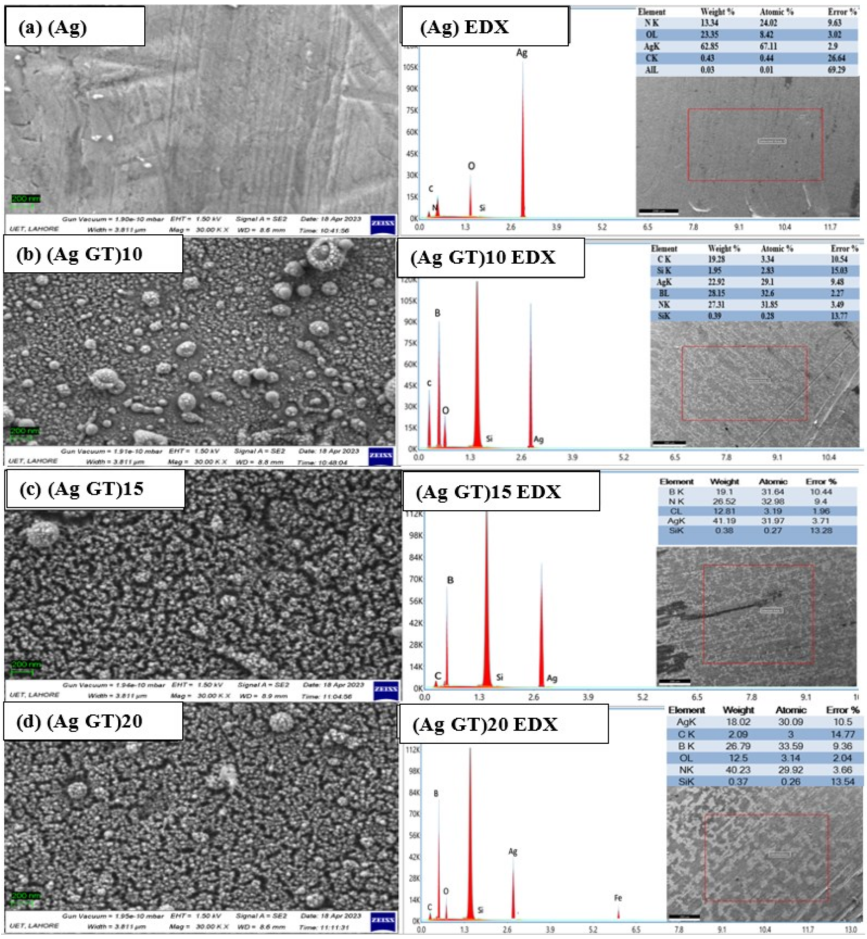

Element	Weight %	Atomic %	Error %
N K	13.34	24.02	9.63
OL	23.35	8.42	3.02
AgK	62.85	67.11	2.9
CK	0.43	0.44	26.64
AlL	0.03	0.01	69.29

Element	Weight %	Atomic %	Error %
C K	19.28	3.34	10.54
Si K	1.95	2.83	15.03
AgK	22.92	29.1	9.48
BL	28.15	32.6	2.27
NK	27.31	31.85	3.49
SiK	0.39	0.28	13.77

Element	Weight	Atomic	Error %
B K	19.1	31.64	10.44
N K	26.52	32.98	9.4
CL	12.81	3.19	1.96
AgK	41.19	31.97	3.71
SiK	0.38	0.27	13.28

Element	Weight	Atomic	Error %
AgK	18.02	30.09	10.5
C K	2.09	3	14.77
B K	26.79	33.59	9.36
OL	12.5	3.14	2.04
NK	40.23	29.92	3.66
SiK	0.37	0.26	13.54

Figure 3. Scanning electron micrographs alongside EDX spectra for **(a)** (Ag); **(b)** (Ag GT)10; **(c)** (Ag GT)15; **(d)** (Ag GT)20.

The FESEM micrographs were processed by software called Fiji ImageJ to evaluate the particle size of BN, porosity of BNNS, and average surface roughness of the grown h-BNNS. **Figure 4** presents the graph of particle size as a function of plasma exposure time while average surface roughness, pore size are functions of plasma exposure time. **Figure 4a** shows a decrease in particle size with extended plasma exposure. The average particle sizes for (Ag GT)10, (Ag GT)15, and (Ag GT)20 are 140.91, 128.43 and 80.66 nm, respectively. Because the highly reactive plasma species break down the larger precursor particles into smaller ones, the particle size decreases with increasing plasma exposure duration. Furthermore, plasma removes impurities and pollutants from the surface, improving h-BNNS growth conditions and encouraging the development of smaller, more uniform BNNS. For (Ag), (Ag GT)10, (Ag GT)15, and (Ag GT)20, the average surface roughness (Ra) values were 23.5337 nm, 31.9465 nm, 47.764 nm, and 43.3627 nm, in that order. An increase in surface roughness was noted for (Ag GT)10 and (Ag GT)15, followed by a decrease for (Ag GT)20. This rise in roughness for (Ag GT)10 is linked to the presence of larger BN particles on these nanosheets. As seen in the earlier graph depicting particle size and growth time (**Figure 4a**,**b**), highly energetic and reactive plasma ions and electrons interacting with Ag and the encroaching fumes of precursor initiate activation processes, leading to increased surface roughness [69,70]. Further enhanced average surface roughness for (Ag GT)15 (**Figure 4b**) is attributed to the presence of the prominent cracks in thusly synthesized h-BNNS (**Figure 3c**). The reduction in average surface roughness for (Ag GT)20 predicts the smoothness of the 2D h-BNNS on Ag. Plasma interaction for a larger time span cleans the surface. This might also be due to the filling of surface defects or voids resulting in a smoother surface. Also, the bigger particles were turned into smaller ones (as seen in SEM section **Figure 3d**). As a result, surface roughness reduced for (Ag GT)20. An observable decrease in porosity with extended plasma exposure time has also been noted (**Figure 4b**). The average pore size reduces a top value of 61.049 to 28.6 nm for (Ag GT)10 and (Ag GT)20 respectively. The highly reactive species from plasma, including ions, excited atoms, electrons, and free radicals, break down bigger covalently SP2-bonded BN particles into smaller ones, which results in the lowering of pore size. This leads to a decrease in pore size because more tiny particles are contained in a smaller volume. Longer plasma exposure causes the boron nitride nanosheets to become more uniform and cover the sample's surface more successfully. As a result, the particle and pore sizes decrease with an increase in plasma exposure time (**Figure 4a**,**b**). Thus, for (Ag GT)20, the average surface roughness is decreased. Thus, in comparison to the other samples, (Ag GT)20 exhibits the most consistent, homogenous, and flexible boron nitride nanosheets.

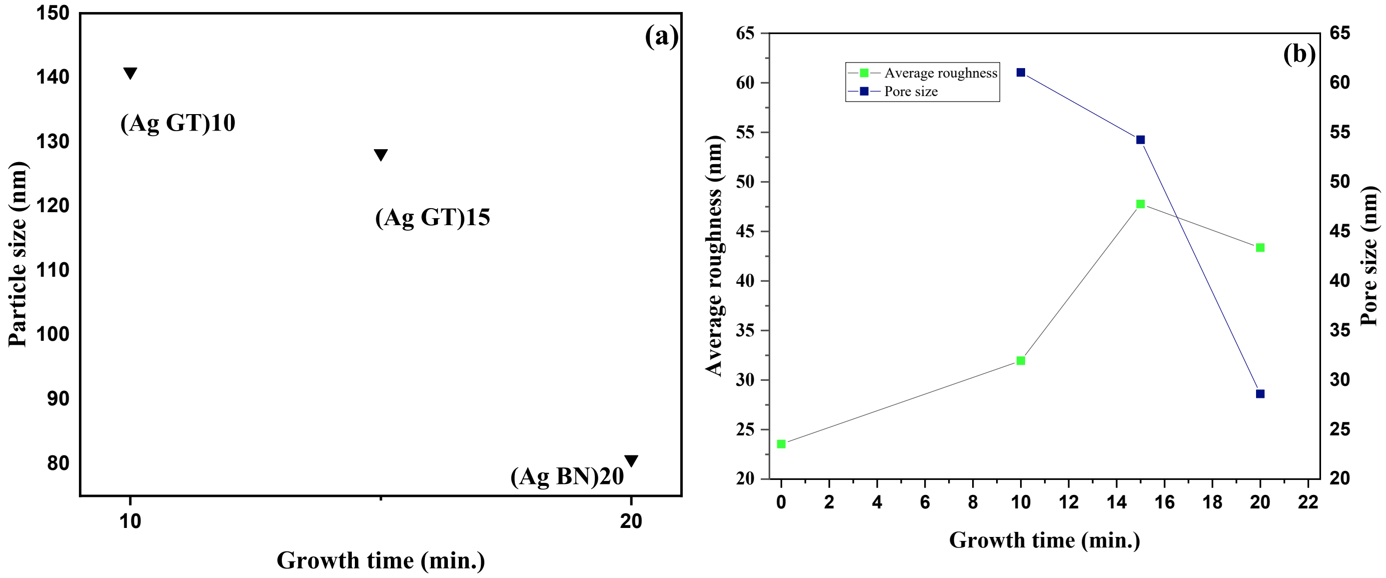

(a) (b)

Figure 4. Graph showing the relationship between **(a)** particle size vs. growth time; **(b)** average surface roughness and pore size vs growth time.

3.3. *X*-ray diffraction analysis

Figure 5 shows the *X*-ray diffraction patterns of (Ag), (Ag GT)10 and (Ag GT)20. The pattern of (Ag GT)15 is missing as our aim was to observe the h-BNNS growth at minimum and maximum plasma exposure time. In the XRD pattern of (Ag) (**Figure 5**), three highly sharp peaks at the positions $2\theta = 38.8°$, 65.2° and 78.6° which represents Ag(111), Ag (220) and Ag(311) respectively (JCPDS Ref. Code 03-065-2871) [71]. For (Ag GT)10 and (Ag GT)20, there are two new peaks at the positions of $2\theta = 26.2°$ and 45.2° which correspond to the h-BN(002) as well as h-BN(100) (JCPDS Ref. Code 00-009-0012) [72,73]. The appearance of these two new peaks confirms the growth of 2D h-BN on Ag via plasma using hexagonal borazine (H_3BNH_3) [74] as a precursor. The borazine contains the stoichiometry 1:1 between B and N [75]. When borazine is used as a precursor, it facilitates the formation of h-BN at reduced temperatures [76]. Before settling down of BN particles from Ar fumes on substrate Ag, electrons and ions from plasma dissociate borazine (H_3BNH_3) into BN accompanied with dehydrogenation [77] according to the Equation (1) given below [78].

$$e^- + H_3BNH_3 \rightarrow BN + 3H_2\uparrow \quad (1)$$

As a result, the dissociated BN readily settles down to the substrate. It is worth noting that despite a large lattice incompatibility between Ag (4.036 Å) [79] and that of h-BN (2.50475 Å) [80], even then there is growth of h-BN on Ag. This is due to the reason that the precursor while interacting with the plasma melts and h-BN dissociates in the molten form. Since plasma is also in direct contact with the Ag substrate as well, it heats up the Ag also. This molten h-BN settles down on the preheated Ag substrate. Consequently, the precursor adheres well to the substrate, leading to more effective growth. Furthermore, the difference in the surface energies of Ag (1.0–2.2 J/m^2) [81] and h-BN (25 mJ/m^2) [50] is less, which is also in favor of this growth. Better wetting is achieved with a fluid with a lower surface tension and a solid with a higher surface energy [82]. Plasma compensates for this lattice mismatch and surface energy difference by improving interfacial interaction between incoming h-BN and the underlying Ag substrate [83]. In the case of (Ag GT)10 as well as (Ag GT)20, it is clearly evident that peaks centered at a diffraction angle of $2\theta = 45.2°$ have slightly higher intensity as compared to peaks situated at $2\theta = 26.2°$ which shows that BN(100) are more abundant/populated than that of BN(002) in the lattice of h-BN [84]. It is also observed that the peaks situated at $2\theta = 26.2°$ and 45.2° for (Ag GT)20 have higher intensity than the corresponding peaks at the same positions in (Ag GT)10 (**Figure 5**). This is because of enhanced plasma-precursor exposure resulting in more effective and improved BN growth. Longer plasma exposure time leads to increased crystallinity [85] by promoting better adhesion, polarization, cleaning, growth and alignment of nanoparticles on Ag substrate that aligns well with literature as well [86]. Also, the crystallite size determined by Scherrer's equation is ~15 nm for (Ag GT)20. Consequently, 20 min. seems to be an optimum growth time at which boron nitride nanosheets can be grown with high crystallinity, high purity and high yield on Ag substrates. It seems reasonable to state that the optimal condition for the growth of h-BNNS on Ag is achieved with plasma operation at 10 kV for 20 min.

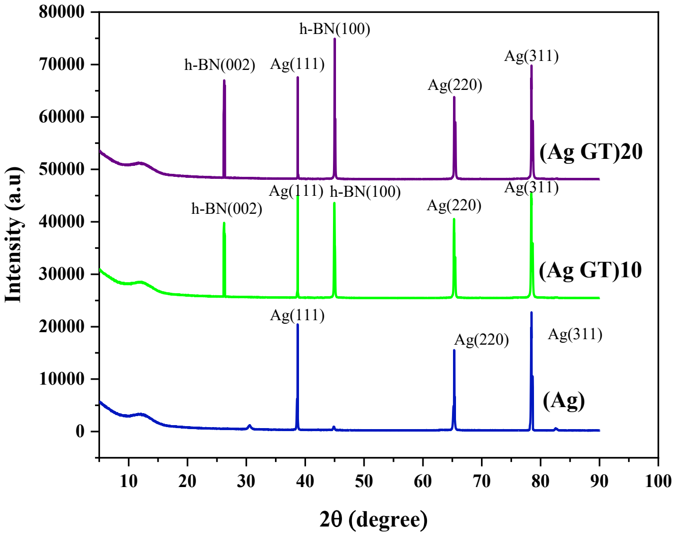

Figure 5. Diffraction peaks observed in *X*-ray analysis of (Ag), (Ag GT)10, and (Ag GT)20.

3.4. Diffuse reflectance spectra analysis

Figure 6 showcases the diffuse reflectance spectra for (Ag), (Ag GT)10, (Ag GT)15, and (Ag GT)20, and a magnified view (360–800 nm) of (Ag), (Ag GT)10, (Ag GT)15, and (Ag GT)20. It appears from the graph that there is no reflection from 200 to 300 nm for all the samples (**Figure 6a**). In this range of the electromagnetic spectrum, all the samples behave as good absorbers. After 300 nm, there is a sharp increase in the reflectivity till 350 nm which lies in the ultraviolet wavelength range. There are two crests corresponding to 550 and 740 nm which show the highest reflectivity for each sample in **Figure 6b**, depicting that these samples are good reflectors for these wavelengths. The curves become smooth from 525 to 675 nm. (Ag) shows maximum reflectivity among (Ag GT)10, (Ag GT)15, (Ag GT)20. The reflectance increases with extended plasma exposure time. As plasma exposure progresses, there is an abrupt decrease in surface roughness of (Ag GT)20 (**Figure 4b**), leading to a smoother surface. Reflectivity for (Ag GT)10 and (Ag GT)15 is lower compared to (Ag) and (Ag GT)20, primarily due to the larger surface particles and surface fractures. The increase in plasma exposure duration introduces new surface chemical groups like C=N, C–C, C≡N, C–H, Ag_2O as well as C=O on the Ag substrate (verified through FT-IR in **Figure 5** as well as EDS analysis in **Figure 3**). Through partial absorption of light and possible modification of reflectance, these newly developed groups alter the way light interacts with the Ag surface.

As the plasma exposure time rises, a decrease in the average particle size was observed (**Figure 4a**). Reflectivity decreases when the particle size gets closer to the wavelength of light due to stronger scattering effects. As demonstrated in **Figure 4b**, the nanosheets formed under similar conditions likewise saw a decrease in pore size with extended plasma exposure. Scattering and interference processes are responsible for influencing overall reflectivity when the wavelength of incident light matches the pore size in the boron nitride nanosheets. As a result, reflectance is reduced. Based on this, (Ag GT)20 seems to be the best sample of the rest of the samples.

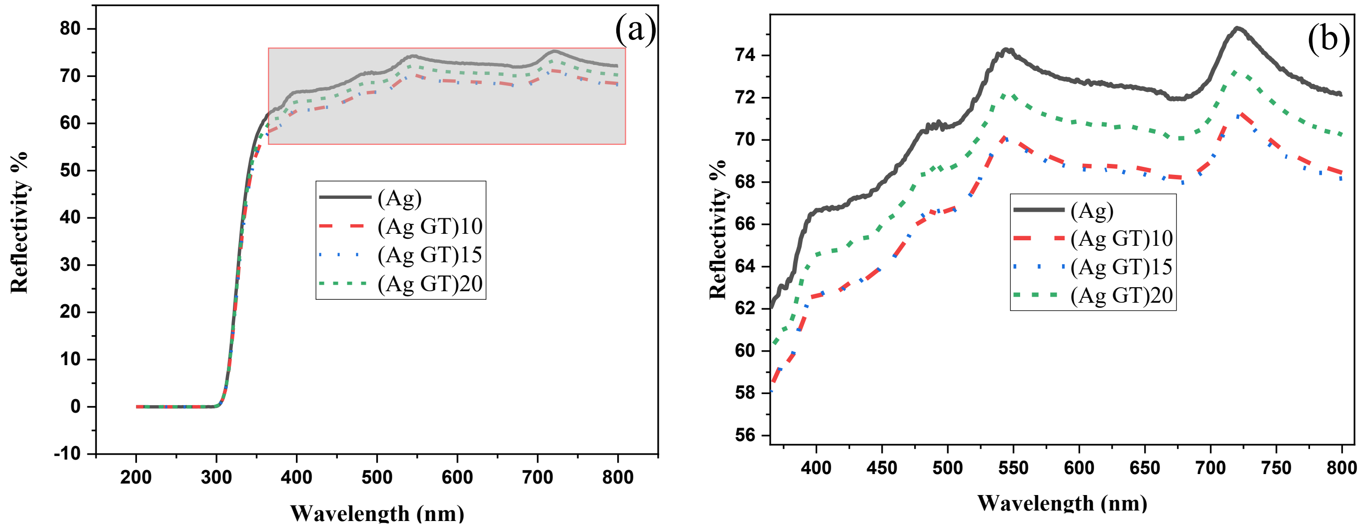

(a) **(b)**

Figure 6. The diffuse reflectance spectra of **(a)** (Ag), (Ag GT)10, (Ag GT)15, and (Ag GT)20; **(b)** a magnified view (360–800 nm) of (Ag), (Ag GT)10, (Ag GT)15, and (Ag GT)20.

3.5. Vickers hardness analysis

Vickers hardness testers with steel balls having a diameter of 1.588 mm and weighing 100 kg were used to measure the hardness of (Ag), (Ag GT)10, (Ag GT)15 and (Ag GT)20 at room temperature. The findings of at least two indentations are averaged to produce the hardness values. **Figure 7** graph illustrates Vickers hardness as a function of plasma exposure time for (Ag), (Ag GT)10, (Ag GT)15, and (Ag GT)20.

From **Figure 7**, it can be concluded that the hardness of each sample shows a near-linear increase with extended plasma exposure time [87,88]. The (Ag) has an average value of 27.6 HV, while the (Ag GT)20 has an average value of 38.3 HV. There is a maximum increase in the hardness of (Ag GT)20 due to the extended plasma exposure episode. This may be due to the increase in hardness when plasma interacts with Ag and BN, leading to cross-linking, ion implantation, and the formation of strong covalent bonds between the substrate and BN. Plasma tends to activate the substrate surface enhancing the adhesion between the substrate and BN particles. Extended plasma exposure duration has also resulted in enhanced crystallinity of (Ag GT)20 (**Figure 3**). With enhanced plasma exposure time, the average pore size as well as the average surface roughness of thusly grown nanosheets has decreased (**Figure 4b**), thus creating a better environment for the adsorbents B and N via cleaning and activating the substrate surface giving rise to hardness. The particle size has also decreased for extended plasma exposure time (as verified in the FESEM section **Figure 4a**). This increase in hardness might also be due to an increase in plasma exposure time resulting in prolonged interaction of radiation like UV, *X*-rays etc., emitted from plasma with the underlying substrate and BN [89,90]. Furthermore, when Ag is exposed to plasma along with precursor borazine, the B and N atoms imbed and penetrate into the Ag surface (as also verified by FT-IR, EDX and XRD techniques) as a result, the hardness of the samples increases. Hence, 20 min and 10 kV are the best optimum parameters to enhance the surface hardness.

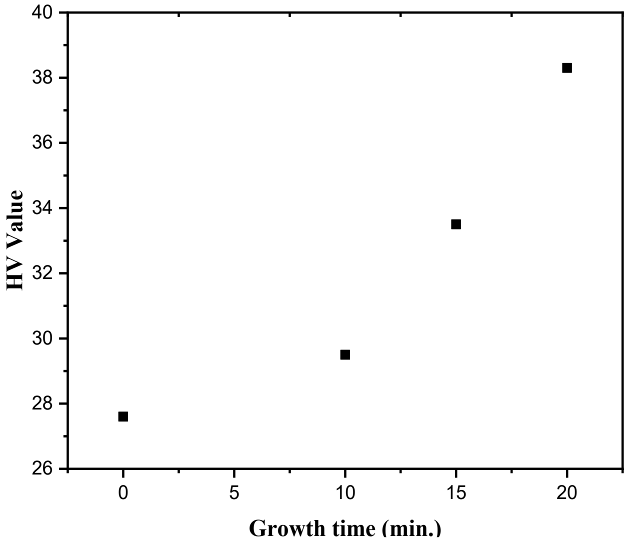

Figure 7. Graph illustrating Vickers hardness as a function of plasma exposure time for (Ag), (Ag GT)10, (Ag GT)15, and (Ag GT)20.

Figure 8 represents the change in the HV value, average particle size, average surface roughness and average pore size versus plasma exposure time of (Ag), (Ag GT)10, (Ag GT)15, (Ag GT)20. It can be inferred from this graph that the average particle size as well as the pore size of boron nitride has reduced with an increase in plasma exposure time. The average surface roughness of the samples increases and then diminishes ultimately for 20 min. interaction time (**Figure 4b**). As a result, the hardness of (Ag), (Ag GT)10, (Ag GT)15, (Ag GT)20 increases from an average 27.6 HV value to a 38.3 HV value [91].

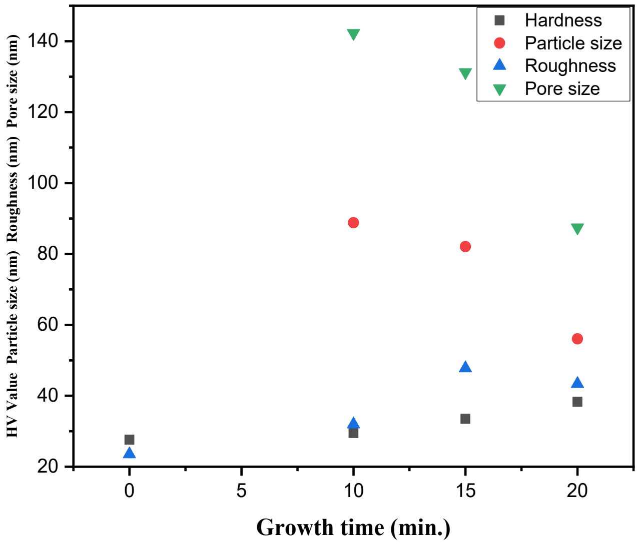

Figure 8. Comparative graph of HV value, average particle size, average surface roughness and average pore size as a function of plasma growth time for samples (Ag), (Ag GT)10, (Ag GT)15, and (Ag GT)20.

4. Conclusion

h-BNNS were synthesized on silver using a simple plasma setup at atmospheric pressure and room temperature. The BN source borazine underwent interaction with the nitrogen plasma for various time spans of 10, 15 and 20 min. h-BNNS are found to be grown for all the plasma exposure times; however, the crystallinity of the grown BN sheets is much better for longer plasma exposure times (20 min. in our case). Smoother nanosheets have grown as a result of a drop in average particle size, average pore size, and average surface roughness as the plasma exposure period has increased. The hardness of the samples has similarly risen with the increase in plasma exposure time.

Therefore, it is concluded that the atmospheric pressure plasma facility serves as an excellent, cost-effective, eco-friendly, and versatile approach for growing h-BNNS on Ag resulting in smoother nanosheets with improved crystallinity and hardness.

Author contributions: Conceptualization, MM and MSR; methodology, MM; software, MM; validation, MK, AA and FS; formal analysis, MA; investigation, IS; resources, FJ and HM; writing—original draft preparation, MM; writing—review and editing, MM; supervision, MSR; project administration, TA. All authors have read and agreed to the published version of the manuscript.

Acknowledgments: The authors express gratitude to the Dean, faculty of Natural Sciences Muhammad Shahid Rafique, at the University of Engineering and Technology Lahore, Pakistan, for overseeing and supervising this study through the research group program. Special thanks are extended to Anwar Latif, Khurram Siraj, Muneeb Irshad, Muhammad Irfan and from the Laser and Optronic Center, Department of Physics, University of Engineering and Technology Lahore, Pakistan, for their valuable contributions.

Institutional review board statement: Not applicable.

Informed consent statement: Not applicable.

Conflict of interest: The authors declare no conflict of interest.

References

1. Wang J, Ma F, Liang W, et al. Electrical properties and applications of graphene, hexagonal boron nitride (h-BN), and graphene/h-BN heterostructures. Materials Today Physics. 2017; 2: 6-34. doi: 10.1016/j.mtphys.2017.07.001
2. Wang S, Li M, Xiang H, et al. A high recognition accuracy tactile sensor based on boron nitride nanosheets/epoxy composites for material identification. Materials Horizons. Published online 2025. doi: 10.1039/d4mh01779j
3. Boldrin L, Scarpa F, Chowdhury R, et al. Effective mechanical properties of hexagonal boron nitride nanosheets. Nanotechnology. 2011; 22(50): 505702. doi: 10.1088/0957-4484/22/50/505702
4. Golberg D, Costa PMFJ, Lourie O, et al. Direct Force Measurements and Kinking under Elastic Deformation of Individual Multiwalled Boron Nitride Nanotubes. Nano Letters. 2007; 7(7): 2146-2151. doi: 10.1021/nl070863r
5. An L, Yu Y, Cai Q, et al. Hexagonal boron nitride nanosheets: Preparation, heat transport property and application as thermally conductive fillers. Progress in Materials Science. 2023; 138: 101154. doi: 10.1016/j.pmatsci.2023.101154
6. Wu W, Zheng M, Lu K, et al. Thermally conductive composites based on hexagonal boron nitride nanosheets for thermal management: Fundamentals to applications. Composites Part A: Applied Science and Manufacturing. 2023; 169: 107533. doi: 10.1016/j.compositesa.2023.107533
7. Yin Z, Bi J, Liang G, et al. Microstructure and mechanical properties of boron nitride nanosheets reinforced eutectic-composition Al2O3/YAG/YSZ composites. Materials Characterization. 2023; 196: 112631. doi: 10.1016/j.matchar.2023.112631
8. Hameed NA, Ali IM, Hassun HK. Calculating surface roughness for a large scale SEM images by mean of image processing. Energy Procedia. 2019; 157: 84-89.
9. Fang H, Bai SL, Wong CP. White graphene"—h-BN based polymeric composites and their application in thermal management. Composites Communications. 2016; 2: 19-24.
10. Fan M, Wang Z, Zhao Y, et al. Porous heterostructure of graphene/hexagonal boron nitride as an efficient electrocatalyst for hydrogen peroxide generation. Carbon Energy. 2022; 5(5). doi: 10.1002/cey2.309
11. Bayramoğlu G, Mudu M. Processing and Characterization of Polypropylene Nanocomposite Films Reinforced with H-BN Nanosheets. Periodica Polytechnica Chemical Engineering. 2023; 67(1): 94-103. doi: 10.3311/PPch.21110
12. Naskar AK, Keum JK, Boeman RG. Polymer matrix nanocomposites for automotive structural components. Nature Nanotechnology. 2016; 11(12): 1026-1030. doi: 10.1038/nnano.2016.262
13. Liu Z, Dibaji A, Li D, et al., Challenges and solutions in surface engineering and assembly of boron nitride nanosheets. Materials Today. 2021; 44: 194-210.
14. Chen Y, Kang Q, Jiang P, et al. Rapid, high-efficient and scalable exfoliation of high-quality boron nitride nanosheets and their application in lithium-sulfur batteries. Nano Research. 2020; 14(7): 2424-2431. doi: 10.1007/s12274-020-3245-3
15. Hayat A, Sohail M, Hamdy MS, et al. Fabrication, characteristics, and applications of boron nitride and their composite nanomaterials. Surfaces and Interfaces. 2022; 29: 101725. doi: 10.1016/j.surfin.2022.101725
16. Deshmukh AR, Jeong JW, Lee SJ, et al. Ultrasound-Assisted Facile Green Synthesis of Hexagonal Boron Nitride Nanosheets and Their Applications. ACS Sustainable Chemistry & Engineering. 2019; 7(20): 17114-17125. doi: 10.1021/acssuschemeng.9b03387
17. Dubey R, Cowles M, Salimi Z, et al. Boron nitride nanosheets, quantum dots, and dots: Synthesis, properties, and biomedical applications. APL Materials. 2025; 13(4). doi: 10.1063/5.0255590
18. Yuan Y, Ru Z, Yi J, et al. Improving the high temperature mechanical properties of boron nitride nanosheet/CuTi composite by increasing grain growth activation energy. Ceramics International. 2025. doi: 10.1016/j.ceramint.2025.03.208
19. Weng Q, Wang X, Wang X, et al. Functionalized hexagonal boron nitride nanomaterials: emerging properties and applications. Chemical Society Reviews. 2016; 45(14): 3989-4012. doi: 10.1039/c5cs00869g
20. Kuang H, Li Y, Huang S, et al. Piezoelectric boron nitride nanosheets for high performance energy harvesting devices. Nano Energy. 2021; 80: 105561. doi: 10.1016/j.nanoen.2020.105561
21. Li LH, Cervenka J, Watanabe K, et al. Strong Oxidation Resistance of Atomically Thin Boron Nitride Nanosheets. ACS Nano. 2014; 8(2): 1457-1462. doi: 10.1021/nn500059s

22. Bhattacharjee A, Jiang H, Li LH, et al. Thermal transport property of boron nitride nanosheets. Applied Physics Reviews. 2024; 11(4). doi: 10.1063/5.0213741
23. Verma A, Parashar A, Packirisamy M. Tailoring the failure morphology of 2D bicrystalline graphene oxide. Journal of Applied Physics. 2018; 124(1). doi: 10.1063/1.5033542
24. Pisharody GR, Sahoo P, Rao DS, et al. Polymer network liquid crystal incorporating a 2D material: Influence of lateral size and concentration of h-BN nanoflakes. Journal of Molecular Liquids. 2025; 418: 126735. doi: 10.1016/j.molliq.2024.126735
25. Cumings J, Zettl A. Field emission and current-voltage properties of boron nitride nanotubes. Solid State Communications. 2004; 129(10): 661-664. doi: 10.1016/j.ssc.2003.11.026
26. Brodu E, Balat-Pichelin M. Emissivity of Boron Nitride and Metals for the Solar Probe Plus Mission. Journal of Spacecraft and Rockets. 2016; 53(6): 1119-1127. doi: 10.2514/1.a33453
27. Chia X, Pumera M. Characteristics and performance of two-dimensional materials for electrocatalysis. Nature Catalysis. 2018; 1(12): 909-921. doi: 10.1038/s41929-018-0181-7
28. Gao Z, Jiang Z, Li J, et al. Anisotropic Mechanics of 2D Materials. Advanced Engineering Materials. 2022; 24(11). doi: 10.1002/adem.202200519
29. Fryauf DM, Phillips AC, Kobayashi NP. Corrosion protection of silver-based telescope mirrors using evaporated anti-oxidation overlayers and aluminum oxide films by atomic layer deposition. Low-Dimensional Materials and Devices 2016. 2016; 9924: 99240S. doi: 10.1117/12.2238749
30. Dean CR, Young AF, Meric I, et al. Boron nitride substrates for high-quality graphene electronics. Nature Nanotechnology. 2010; 5(10): 722-726. doi: 10.1038/nnano.2010.172
31. Cai Q, Li LH, Mateti S, et al. Boron Nitride Nanosheets: Thickness-Related Properties and Applications. Advanced Functional Materials. 2024; 34(40). doi: 10.1002/adfm.202403669
32. Yu R, Yuan X. Rising of boron nitride: A review on boron nitride nanosheets enhanced anti-corrosion coatings. Progress in Organic Coatings. 2024; 186: 107990. doi: 10.1016/j.porgcoat.2023.107990
33. Hossain K, Ahmed MT, Rabu RA, et al. First-principles investigations of As-doped tetragonal boron nitride nanosheets for toxic gas sensing applications. Nanoscale Advances. 2025; 7(1): 354-369. doi: 10.1039/d4na00739e
34. Shelimov KB, Moskovits M. Composite Nanostructures Based on Template-Grown Boron Nitride Nanotubules. Chemistry of Materials. 1999; 12(1): 250-254. doi: 10.1021/cm9905996
35. Golberg D, Bando Y, Kurashima K, et al. Nanotubes of Boron Nitride Filled with Molybdenum Clusters. Journal of Nanoscience and Nanotechnology. 2001; 1(1): 49-54. doi: 10.1166/jnn.2001.008
36. Ma R, Bando Y, Sato T. Coaxial nanocables: Fe nanowires encapsulated in BN nanotubes with intermediate C layers. Chemical physics letters. 2001; 350(1-2): 1-5.
37. Chen X, Wu P, Rousseas M, et al. Boron Nitride Nanotubes Are Noncytotoxic and Can Be Functionalized for Interaction with Proteins and Cells. Journal of the American Chemical Society. 2009; 131(3): 890-891. doi: 10.1021/ja807334b
38. Doğan M, Selek A, Turhan O, et al. Different functional groups functionalized hexagonal boron nitride (h-BN) nanoparticles and multi-walled carbon nanotubes (MWCNT) for hydrogen storage. Fuel. 2021; 303: 121335. doi: 10.1016/j.fuel.2021.121335
39. Kim KB, Jang W, Cho JY, et al. Transparent and flexible piezoelectric sensor for detecting human movement with a boron nitride nanosheet (BNNS). Nano Energy. 2018; 54: 91-98. doi: 10.1016/j.nanoen.2018.09.056
40. Cumings J, Zettl A. Field emission and current-voltage properties of boron nitride nanotubes. Solid State Communications. 2004;129(10): 661-664.
41. Fu M, Yu H, Chen W. Construction of Co3O4 porous rod/graphene heterostructures toward strong and broadband microwave absorption applications. Applied Surface Science. 2023; 622: 156946.
42. Biswas A, Ruan Q, Lee F, et al. Unidirectional domain growth of hexagonal boron nitride thin films. Applied Materials Today. 2023; 30: 101734. doi: 10.1016/j.apmt.2023.101734
43. Kubota Y, Watanabe K, Tsuda O, et al. Deep Ultraviolet Light-Emitting Hexagonal Boron Nitride Synthesized at Atmospheric Pressure. Science. 2007; 317(5840): 932-934. doi: 10.1126/science.1144216
44. Watanabe K, Taniguchi T, Kanda H. Direct-bandgap properties and evidence for ultraviolet lasing of hexagonal boron nitride single crystal. Nature Materials. 2004; 3(6): 404-409. doi: 10.1038/nmat1134
45. Li, Q. Anisotropic Mechanical Properties of 2-D Materials. In Material Flow Analysis. IntechOpen. 2021. doi: 10.5772/intechopen.96598

46. Grassini S, Angelini E, Mao Y, et al. Aesthetic coatings for silver based alloys with improved protection efficiency. Progress in Organic Coatings. 2011; 72(1-2): 131-137. doi: 10.1016/j.porgcoat.2011.04.003
47. Zhang L, Li X, Shao Y, et al. Improving the quality of GaN crystals by using graphene or hexagonal boron nitride nanosheets substrate. ACS applied materials & interfaces. 2015; 7(8): 4504-4510. doi: 10.1021/am5087775
48. Jiang H, Cai Q, Mateti S, et al. Boron Nitride Nanosheet Dispersion at High Concentrations. ACS Applied Materials & Interfaces. 2021; 13(37): 44751-44759. doi: 10.1021/acsami.1c11795
49. Vijayaraghavan V, Zhang L. Effective mechanical properties and thickness determination of boron nitride nanosheets using molecular dynamics simulation. Nanomaterials. 2018; 8(7): 546. doi: 10.3390/nano8070546
50. Wu M, Gao J, Dai W, et al. A mini review of flexible heat spreaders based on functionalized boron nitride nanosheets. ASME Journal of Heat and Mass Transfer. 2025; 147(3). doi: org/10.1115/1.4067474
51. Gay PA, Bercot P, Pagetti J. The protection of silver against atmospheric attack. Plating and surface finishing. 2004; 91(5): 71-73
52. Hagans PL, Haas CM. Chromate Conversion Coatings. Surface Engineering. 1994; 405-411. doi: 10.31399/asm.hb.v05.a0001275
53. Chen C, Yu B, Jia H, et al. Efficient Preparation of Hydrophilic Boron Nitride Nanosheets for Human Heat Dissipation Applications. ACS Applied Nano Materials. 2024; 7(10): 11487-11497. doi: org/10.1021/acsanm.4c01100
54. Roudi MRR, Ranjkesh M, Korayem AH, Shahsavary R. Review of boron nitride nanosheet-based composites for construction applications. ACS Applied Nano Materials. 2022; 5(12): 17356-17372. doi: 10.1021/acsanm.2c03200
55. Zhang Y, Du H, Ma Y, et al. Hexagonal boron nitride nanosheet for effective ambient N2 fixation to NH3. Nano Research. 2019; 12(4): 919-924. doi: 10.1007/s12274-019-2323-x
56. Petrelli C, Goos A, Ruhlandt-Senge K, Spencer JT. Functionalization of boron nitride nanosheets (BNNSs) by organic polymers: formation of substituted polythiophene–BNNS structures. Journal of Materials Science. 2016; 51: 4952-4962. doi: 10.1007/s10853-016-9800-3
57. Müller F, Hüfner S, Sachdev H, et al. Epitaxial growth of hexagonal boron nitride on Ag(111). Physical Review B. 2010; 82(11). doi: 10.1103/physrevb.82.113406
58. Garnica M, Schwarz M, Ducke J, et al., Comparative study of the interfaces of graphene and h-BN with silver. Physical Review B. 2016; 94(15): 155431.
59. Han R, Khan MH, Angeloski A, et al. Hexagonal Boron Nitride Nanosheets Grown via Chemical Vapor Deposition for Silver Protection. ACS Applied Nano Materials. 2019; 2(5): 2830-2835. doi: 10.1021/acsanm.9b00298
60. Li LH, Xing T, Chen Y, et al. Boron Nitride Nanosheets for Metal Protection. Advanced Materials Interfaces. 2014; 1(8). doi: 10.1002/admi.201300132
61. Corso M, Auwärter W, Muntwiler M, et al. Boron Nitride Nanomesh. Science. 2004; 303(5655): 217-220. doi: 10.1126/science.1091979
62. Goriachko A, He, Knapp M, et al. Self-Assembly of a Hexagonal Boron Nitride Nanomesh on Ru(0001). Langmuir. 2007; 23(6): 2928-2931. doi: 10.1021/la062990t
63. Rohr C, Boo JH, Ho W. The growth of h-BN thin films on silicon using single source precursor. Thin Solid Films. 1998; 322(1-2): 9-13.
64. Deng JX, Zhang XK, Qian Y, et al. Optical properties of hexagonal boron nitride thin films deposited by radio frequency bias magnetron sputtering. Chinese Physics B. 2009; 18(9): 4013-4018. doi: 10.1088/1674-1056/18/9/066
65. Du M, Wu Y, Hao X. A facile chemical exfoliation method to obtain large size boron nitride nanosheets. CrystEngComm. 2013; 15(9): 1782. doi: 10.1039/c2ce26446c
66. Wang N, Yang G, Wang H, et al. A universal method for large-yield and high-concentration exfoliation of two-dimensional hexagonal boron nitride nanosheets. Materials Today. 2019; 27: 33-42. doi: 10.1016/j.mattod.2018.10.039
67. Sainsbury T, Satti A, May P, et al. Oxygen Radical Functionalization of Boron Nitride Nanosheets. Journal of the American Chemical Society. 2012; 134(45): 18758-18771. doi: 10.1021/ja3080665
68. Berner S, Corso M, Widmer R, et al. Boron nitride nanomesh: Functionality from a corrugated monolayer. Angewandte Chemie international edition. 2007; 46(27): 5115-5119. doi: 10.1002/anie.200700234
69. Zhi C, Bando Y, Tang C, Golberg D. Boron nitride nanotubes. Materials Science and Engineering: R: Reports. 2010; 70(3-6): 92-111. doi: 10.1016/j.mser.2010.06.004
70. Zheng X, Wu K, Zhan Y, et al. Heterostructured Alumina/Boron Nitride Nanosheets for Thermal Management of

Poly(dimethylsiloxane). ACS Applied Nano Materials. 2024; 7(10): 11803-11815. doi: 10.1021/acsanm.4c01401

71. Nadeem MS, Baoji M, Alam MM, et al. Sr-doped ZnO thin film on a silicon substrate (100) grown by sol-gel method: Structural and optical study. Optical Materials. 2024; 157: 116106. doi: 10.1016/j.optmat.2024.116106
72. Nazarov AS, Demin VN, Grayfer ED, et al. Functionalization and Dispersion of Hexagonal Boron Nitride (h-BN) Nanosheets Treated with Inorganic Reagents. Chemistry – An Asian Journal. 2012; 7(3): 554-560. doi: 10.1002/asia.201100710
73. Shi Y, Hamsen C, Jia X, et al. Synthesis of Few-Layer Hexagonal Boron Nitride Thin Film by Chemical Vapor Deposition. Nano Letters. 2010; 10(10): 4134-4139. doi: 10.1021/nl1023707
74. Islas R, Chamorro E, Robles J, et al. Borazine: to be or not to be aromatic. Structural Chemistry. 2007; 18(6): 833-839. doi: 10.1007/s11224-007-9229-z
75. Seghi S, Lee J, Economy J. High density carbon fiber/boron nitride matrix composites: Fabrication of composites with exceptional wear resistance. Carbon. 2005; 43(10): 2035-2043. doi: 10.1016/j.carbon.2005.02.033
76. Demin VN, Asanov IP, Akkerman ZL. Chemical vapor deposition of pyrolytic boron nitride from borazine. Journal of Vacuum Science & Technology A: Vacuum, Surfaces, and Films. 2000; 18(1): 94-98. doi: 10.1116/1.582124
77. Bachmann P, Düll F, Späth F, et al. A HR-XPS study of the formation of h-BN on Ni(111) from the two precursors, ammonia borane and borazine. The Journal of Chemical Physics. 2018; 149(16). doi: 10.1063/1.5051595
78. Konyashin I, Bill J, Aldinger F. Plasma-assisted CVD of cubic boron nitride. Chemical Vapor Deposition. 1997; 3(5): 239-255. doi: 10.1002/cvde.19970030502
79. Rao CN, Rao KK. Effect of temperature on the lattice parameters of some silver—palladium alloys. Canadian Journal of Physics. 1964; 42(7): 1336-1342. doi: 10.1139/p64-120
80. Paszkowicz W, Pelka JB, Knapp M, et al. Lattice parameters and anisotropic thermal expansion of hexagonal boron nitride in the 10–297.5 K temperature range. Applied Physics A: Materials Science & Processing. 2002; 75(3): 431-435. doi: 10.1007/s003390100999
81. Medasani B, Park YH, Vasiliev I. Theoretical study of the surface energy, stress, and lattice contraction of silver nanoparticles. Physical Review B. 2007; 75(23). doi: 10.1103/physrevb.75.235436
82. Roy S, Zhang X, Puthirath AB, et al. Structure, Properties and Applications of Two-Dimensional H-BN. Adv Mater. 2021; 33(44): e2101589
83. Ji T, Zhang L, Wang W, et al. Cold plasma modification of boron nitride fillers and its effect on the thermal conductivity of silicone rubber/boron nitride composites. Polymer Composites. 2012; 33(9): 1473-1481. doi: 10.1002/pc.22277
84. Nadeem MS, Munawar T, Alam MM, et al. Effect of Co/Nd co-doping on the structural, optical, and morphological properties of ZnO nanorods grown on silicon substrate Si (100) by hydrothermal method. Journal of Luminescence. 2024; 269: 120484. doi: 10.1016/j.jlumin.2024.120484
85. Achour H, Achour A, Solaymani S, et al. Plasma surface functionalization of boron nitride nano-sheets. Diamond and Related Materials. 2017; 77: 110-115. doi: 10.1016/j.diamond.2017.06.012
86. Thurston RM, Clay JD, Schulte MD. Effect of Atmospheric Plasma Treatment On Polymer Surface Energy and Adhesion. Journal of Plastic Film & Sheeting. 2007; 23(1): 63-78. doi: 10.1177/8756087907078698
87. Qureshi A, Shah S, Pelagade S, et al. Surface modification of polycarbonate by plasma treatment. Journal of Physics: Conference Series. 2010; 208: 012108. doi: 10.1088/1742-6596/208/1/012108
88. Gibeop N, Lee DW, Prasad CV, et al. Effect of plasma treatment on mechanical properties of jute fiber/poly (lactic acid) biodegradable composites. Advanced Composite Materials. 2013; 22(6): 389-399. doi: 10.1080/09243046.2013.843814
89. Turcu IE, Dance JB. X-rays from laser plasmas: generation and applications. Wiley-VCH; 1998.
90. Ahmad AN, Rafique MS, Arslan M, et al. Emission of ions and electrons correlated with soft and hard x-rays evolution from thermal plasma. Physics of Plasmas. 2024; 31(5). doi: 10.1063/5.0197805
91. Mudassar M, Rafique MS, Naveed A, et al. Atmospheric pressure plasma-assisted growth of hexagonal boron nitride nanosheets for improved aluminum hardness. Diamond and Related Materials. 2024; 145: 111076. doi: 10.1016/j.diamond.2024.111076